The Hebrew University of Jerusalem
Faculty of Mathematics and Sciences
Selim and Rachel Benin School of Engineering
Applied Physics Department

Sub-GHz Resolution Adaptive Filter and Flexible Shaping Photonic Spectral Processor

מעצב אופטי בעל כושר הפרדה תת-ג'יגה הרץ

by

Roy Rudnick

This work was done under the supervision of

Prof. Dan M. Marom

Thesis submitted for a M.Sc. degree

December, 2014

Abstract

A record performance metric arrayed waveguide grating (AWG) design with a 200 GHz free spectral range (FSR) capable of resolving sub-one GHz resolution spectral features is developed for a fine resolution photonic spectral processor (PSP). The AWG's FSR was designed to support sub-channel add/drop from a super-channel of 1Tb/s capacity. Due to fabrication imperfections we introduce phase corrections to the light beams emerging from the 250 waveguides of the AWG output using a liquid crystal on Silicon (LCoS) phase spatial light modulator (SLM) placed in an imaging configuration. A second LCoS SLM is located at the Fourier plane, for arbitrary spectral amplitude and phase manipulations. The PSP is utilized in different experiments, such as flexible spectral shaping and sub-carrier drop demultiplexer with sub-GHz spectral resolution.

תקציר

עיצוב מערך מוליכי גלים (AWG) בעל חלון ספקטרלי מחזורי של 200 גיגה הרץ המאפשר מניפולציות ספקטרליות עם כושר הפרדה תת גיגה הרץ פותח בשביל מעבד ספקטרלי בעל רזולוציה חדה. החלון הספקטרלי תוכנן כך שיוכל לתמוך בהעלאה והורדה של תת ערוצים מערוץ על עם קיבולת של 1 טרה-ביט לשנייה. עקב פגמים ביצור נציג תיקוני פאזה לקרני אור היוצאים מה250 מוליכי גלים של AWG בעזרת גביש נוזלי על סיליקון המשמש כמאפנן פאזה אופטי המוקם במערכת במישור הדמיה. בעזרת מאפנן פאזה אופטי נוסף המוקם במערכת במישור פורייה נבצע שינוי משרעת ופאזה ספקטרליים שרירותיים. המעבד האופטי מנוצל בניסוים למטרת עיצוב ספקטרלי ופיצול תתי ערוצים ברזולוציה חדה שלא נראה עד כה.

Acknowledgments

I would like to thank Prof. Dan M. Marom for his guidance throughout my research and passing down helpful knowledge of optical systems.

Also I would like to thank all the members of our photonic lab group: Miri Blau, Yedidya Lior, Moran Bin-Nun, David Sinefeld, Ori Golani and Leonid Pascar for their helpful support whether it was theoretical, technical or any miscellaneous help.

Thanks! Without you guys I couldn't have succeeded…

Contents

1. Introduction

Linear optical signal processing operations can assist optical communications in performing myriads of operations such as wavelength multiplexing, wavelength selective switching (WSS), and complex spectral filtering for channel selection, dispersion compensation, and signal shaping. Adaptive filtering operations are particularly of interest, enabling tuning of the center wavelength, selected bandwidth, dispersion compensation level and signal format conversion. Performing these operations with a spatial light modulator (SLM) operating on spatially dispersed light has been demonstrated [1-3]. These and similar experiments are based on a WSS platform, using a dispersive free-space optics arrangement with a bulk diffraction grating and lenses, and replacing a micro-mirror SLM [4] with a liquid crystal on silicon (LCoS) SLM for finer control [5]. The performance of these WSS based instruments is set by the spectral resolution of the dispersing arrangement (typically 5-10 GHz) and the pixel pitch determining spectral addressability (few GHz). As such, their performance attributes fall short of those required to optimally support intra-channel filtering requirements in telecom applications. Improved optical resolution metrics can be obtained by replacing the bulk diffraction grating with an arrayed waveguide grating (AWG) [6, 7] or a virtually imaged phased array (VIPA) [8], both of which can be designed to provide larger dispersion values over a finite free spectral range (FSR). These larger dispersion devices provide finer optical resolution for intra-channel spectral filtering, giving the filtering apparatus the moniker photonic spectral processor (PSP). Our PSP is based on a hybrid guided wave and free-space optics arrangement, where the AWG, implemented in silica waveguides, disperses the light. The diffracted light is then focused by a Fourier lens onto an LCoS, two-dimensional phase SLM. With the LCoS SLM we are able to prescribe phase and amplitude onto the signal's spatially dispersed spectral components. In this thesis, we vastly improve the fine-resolution filtering attributes of an AWG based PSP.

Our new PSP implementation is based on an AWG designed to obtain 0.8 GHz optical resolution over a 200 GHz FSR. Similar resolution was demonstrated before for an AWG demultiplexer (demux) over a 16 GHz FSR [9]. Obtaining such resolution attributes requires very large delays within the AWG, while still maintaining phase accuracy at the output. Unfortunately, these requirements are beyond standard fabrication tolerances, resulting in the AWG having excessive phase errors which completely ruin the constructive phased array interference at the output. In [9], individual waveguides were phase trimmed with ultra-violet (UV) irradiation after Hydrogen loading. We employed a phase compensation technique based on a phase SLM to correct the individual waveguide's phase errors and obtain the true optical resolution of the fabricated AWG. The record performance metrics of the PSP allow synthesizing complex spectral filtering functions with extremely sharp features nearly matching ideal characteristics.

2 Background

2.1 Controlling Spectral Elements with a Photonic Spectral Processor

In order to control optical signals, it is possible to apply phase and amplitude manipulations in the spectral domain. In this way it is possible to filter out desired or undesired spectral components and signal shaping, whether it is to compensate phase dispersion or amplitude impairments. For instance carving spectral components so that they all have the same amplitude.

Achieving all of the above with one device can be done within a system called a photonic spectral processor (PSP). This system is based on dispersion devices which provide angular dispersion to separate the optical signal's frequency components that radiate out from an input fiber. Followed by a Fourier lens transforming the angular dispersion to spatial dispersion in the spectral plane. Placed in the spectral plane is a spatial light modulator (SLM) which has the ability to manipulate the spectrally resolved signal by applying amplitude functions with or without phase functions or vice versa. The manipulated signal in the spectral domain is then coupled to an output fiber port, this can be seen in Fig. 2.1.1

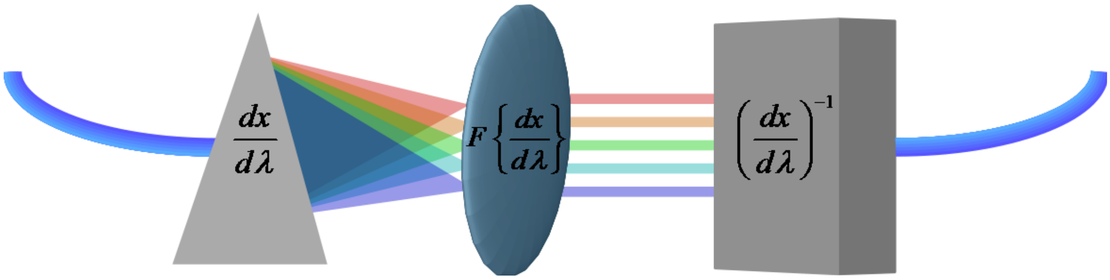

Fig. 2.1.1 – A depiction of a Photonic Spectral Processor concept. An input fiber careering an optical signal is coupled to an angular dispersion element which forms a spectral spread of the signal in the spectral plane by a Fourier lens. Placed in this plane is a spatial light modulator enabling phase and amplitude modulation for each spectral component. The manipulated signal is then coupled to an output fiber.

The PSP presented in this work is based on a hybrid guided wave and free-space optics arrangement, where an arrayed waveguide grating (AWG), implemented in silica waveguides, disperses the light. The diffracted light is then focused by a Fourier lens onto a liquid crystal on Silicon (LCoS), two-dimensional phase SLM. With the LCoS SLM we are capable of phase and amplitude manipulation, the latter done by writing on the LCoS SLM a linear phase ramp diverting a certain percentage of the light out of the optical path for a desired amplitude attenuation. In this way we are able to prescribe phase and amplitude onto the signal's spatially dispersed spectral components (Fig. 2.1.2).

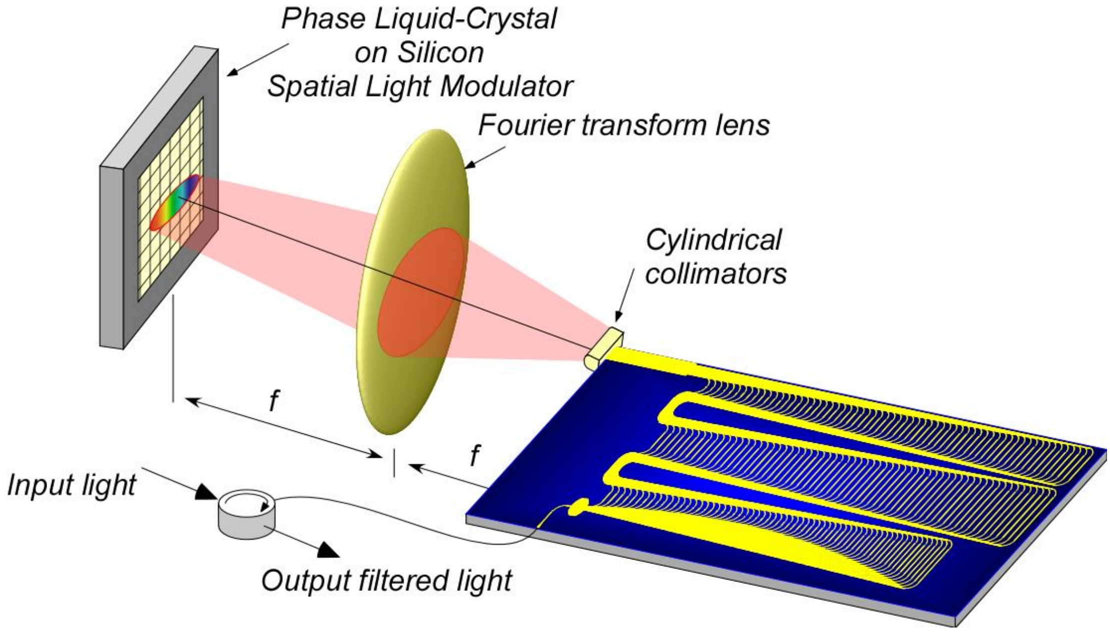

Fig. 2.1.2 – A hybrid guided wave and free-space optics PSP. An input fiber is connected to an optical circulator which is connected to a fiber that is coupled to an AWG angular dispersion element. The radiating light is collimated via cylindrical lens. The angular dispersion is transformed to spatial dispersion by a Fourier lens. In the spectral plane an LCoS SLM is placed enabling phase and amplitude modulation. The signal is coupled back to the circulator flowing in the opposite direction on the same input fiber.

In order to manifest a PSP with fine optical performance capable of applying sharp adaptive optical functions on an optical signal, two key aspects need to be addressed. One being the spectral resolution which is dependent on the dispersive element. The other being the spectral addressability, which depends on the SLM technology. These two aspects will be explained more in detail in the following chapter.

2.2 Resolution and Addressability of a PSP

The hallmark of a PSP is its spectral resolution, hence it is important to define this metric and how it can be experimentally assessed. The optical resolution of the PSP is one of the key elements effecting the channel passband characteristics. A finer resolution PSP will provide a wider passband characteristic across the allocated channel bandwidth on a SLM pixels. This is due to more abrupt transitions from pass to block bands as a result of finer filtering. This is instrumental for densely packing channels in the telecom optical window (1530-1565 nm) dictated by current optical amplification technology. In other words minimizing the guard bandwidth required between channels which is roughly equivalent to the transition bandwidth from pass to block bands. These guard bands are necessary otherwise coherent crosstalk will arise.

Let us now consider the spectral response in an analytic fashion. The dispersed optical signal can be described by Eq. (2.2.1), which describes a space (x)-temporal frequency (v) mixed signal (for simplicity we restrict the analysis to one dimension (ignoring the y-axis dependence). Each spectral component is focused to a spot size of $2w_0$ at a unique position, and the spectra is linearly dispersed as defined by dx/dv.

$$\varphi(x;\nu) = \exp\left[-\left(x - \frac{dx}{d\nu}(\nu - \nu_0) \right)^2 \Big/ w_0^2 \right] \tag{2.2.1}$$

We propose to define the spectral resolution as the ratio relating the beam size and the spatial dispersion, according to $v_{res} = w_0/(dx/dv)$. We next prove this spectral resolution metric is sensible for assessing the performance of a PSP.

Let the SLM select a spatial extent Δx about x_c (the position of center frequency v_c). Performing the overlap integral over the spatial coordinate x, yields the coupling strength for every spectral component [4]:

$$|\eta(\nu)|^2 = \frac{1}{4}\left(\operatorname{erf}\left[\frac{\sqrt{2}}{w_0}\left(\frac{\Delta x}{2} + \frac{dx}{d\nu}(\nu_c - \nu_0) \right) \right] + \operatorname{erf}\left[\frac{\sqrt{2}}{w_0}\left(\frac{\Delta x}{2} - \frac{dx}{d\nu}(\nu_c - \nu_0) \right) \right] \right)^2 \tag{2.2.2}$$

where erf(•) is the error function. Substituting $\Delta x = (dx/dv)\cdot\Delta v$ and using our resolution definition for v_{res}, we obtain

$$\left|\eta(\nu)\right|^2 = \frac{1}{4}\left(\mathrm{erf}\left[\frac{\sqrt{2}}{\nu_{res}}\left(\frac{\Delta\nu}{2}+(\nu-\nu_c)\right)\right]+\mathrm{erf}\left[\frac{\sqrt{2}}{\nu_{res}}\left(\frac{\Delta\nu}{2}-(\nu-\nu_c)\right)\right]\right)^2 \qquad (2.2.3)$$

Each error function in Eq. (2.2.3) defines the spectral roll-off at the corresponding spectral edge. Under the assumption that the two edges do not overlap (which occurs for sufficiently large bandwidth selection, $\Delta\nu$, relatively to ν_{res}), then each error function defines the edge roll-off independently. Many metrics may be used to assess the roll-off from the pass-band to the block-band. Using the 90%-10% transition seen in Fig. 2.2.1 - left (analogous to -0.5 dB to -10 dB transition), we evaluate the erf(•) values in Eq. (2.2.3) leading to the target measures, and find that the difference in the two arguments is 1.436. Hence the transition occurs over a bandwidth of $1.436\cdot\nu_{res}/\sqrt{2}\approx\nu_{res}$. The 90-10 transition bandwidth is easy to identify and measure (Fig. 2.2.1) and is equivalent to directly measuring the dispersing optics′ resolution. Likewise, we can also predict the transition from -0.5dB down to –20 dB ($1.4\cdot\nu_{res}$) and down to -30 dB ($1.667\cdot\nu_{res}$) seen in Fig. 2.2.1-right. If we wish to maintain -40dB isolation between adjacent channel components we can adopt a $1.9\cdot\nu_{res}$ metric for wavelength division multiplexing (WDM) signal separation, which can be rounded to $2\cdot\nu_{res}$ for the transition bandwidth between two separate channels (with a safety margin).

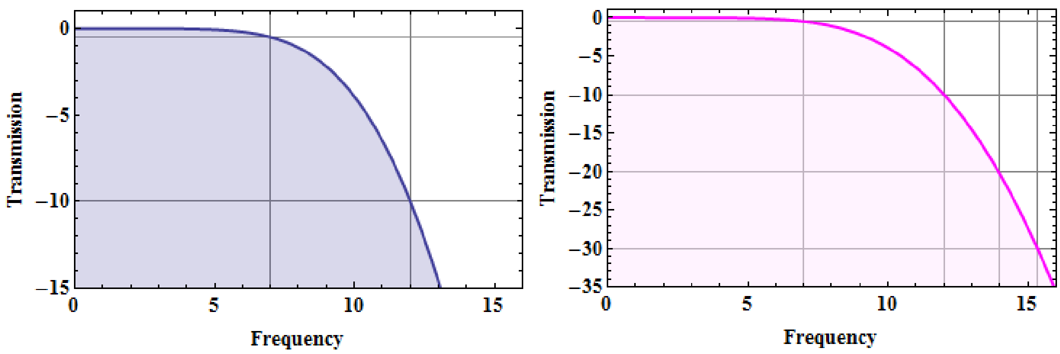

Fig. 2.2.1 – Characterizing the optical resolution of the filter shape, by measuring the bandwidth for the transition from -0.5 dB to -10 dB (equivalent to the 90-10 drop bandwidth). (Left) Horizontal grid lines at -0.5 dB and -10 dB, demonstrating a 5 dB optical resolution (from 7 GHz to 12 GHz). (Right) Additional measures added at -20 dB and -30 dB, at 1.4×5=7 GHz, and 1.66×5=8.33 GHz.

In addition to the resolution metric, a PSP is also characterized by the positional accuracy at which it is possible to encode a spectral function on the SLM. This positional accuracy is defined by the spectral addressability. Knowing the spatial dispersion term and SLM pixel size, the spectral addressability is (*SLM pixel size*)/(*dx*/*dv*).

To summarize, the spectral addressability at which channel bandwidths can be assigned is defined by the SLM size and the spatial dispersion, whereas the channel passband shape is determined by the optical resolution.

All that has been defined in this section is depicted in Fig. 2.2.2, where different channel bandwidths have been reconfigured at a spectral addressability of 6.25 GHz and the response for various optical resolution values (7.5, 5, and 2.5 GHz) is shown. Two elevation lines, showing -3dB pass bandwidth and -35dB block bandwidth also shown. The region in between is generally reserved for guard bands when transmitting information, and this wasted region is reduced for higher resolution PSP.

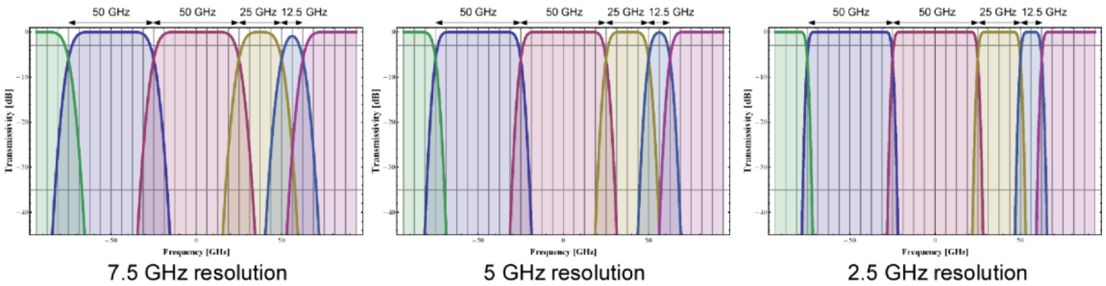

Fig. 2.2.2 – Calculated PSP spectral performance characteristics, when variable bandwidth channels are deployed at spectral granularity of 6.25 GHz (denoted by vertical grid lines). The three cases shown correspond to optical resolution of 7.5 GHz, 5 GHz, and 2.5 GHz.

2.3 Liquid Crystal on Silicon Spatial Light Modulator

Current spatial light modulator technologies which enables the amplitude and phase control for each wavelength component include micro electro-mechanical systems (MEMS) [10-12] and liquid crystal on Silicon (LCoS) [13] modulators (Fig. 2.3.1). The latter consisting of a larger number of pixels with respective smaller pixel size, resulting in resolving spectral features with a finer resolution. In addition LCoS unlike MEMES is commercially available, hence we opted for LCoS SLM technology.

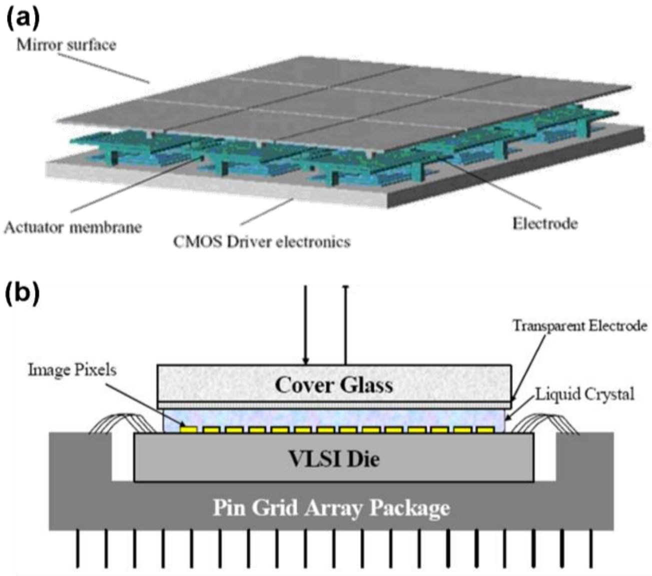

Fig. 2.3.1 – MEMS and LCoS Phase SLM schematic drawings (a) MEMS based phase SLM: by applying voltage with a complementary metal oxide semiconductor (CMOS) electronic driver, an actuator drives a pixelated mirror up and down up to a λ/2 travel. (b) LCoS based phase SLM: a layer of liquid crystals is placed between a transparent electrode and a very large scale integration (VLSI) die of two dimensional array of pixels. Different voltage values applied separately on each SLM pixel result in different local index of refraction. This change is equal to a change in the optical path length and therefore to a phase delay.

The operation method of the LCoS SLM is based on a liquid crystal (LC) layer which lies between a transparent electrode and a VLSI die. When voltage is applied on a specific pixel, LC molecules in the pixel area rotate in order to align along the lines of the electrical field (Fig. 2.3.2). The LC molecules angular orientation is dependent on the applied voltage according to [14]:

$$\theta = \frac{\pi}{2} - 2 \cdot \arctan(\mathrm{e}^{-V}) \qquad (2.3.1)$$

Since LC molecules are elliptic, their rotation effect the index ellipsoid according to:

$$\frac{1}{n(\theta)^2} = \frac{\cos^2(\theta)}{n_0^2} + \frac{\sin^2(\theta)}{n_e^2} \qquad (2.3.2)$$

where n_o and n_e are the refraction index of the ordinary and extra-ordinary axis respectively. The phase that each pixel can apply is therefore given by:

$$\phi = \frac{2\pi}{\lambda}\left(n(V) - n_0\right) \qquad (2.3.3)$$

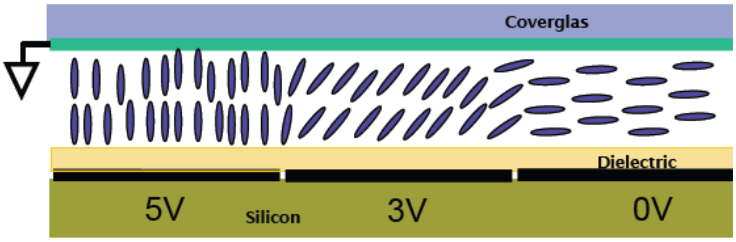

Fig. 2.3.2 – LCoS Phase SLM basic concept of operation: The layer of liquid crystals rotates according to the applied voltage, resulting in a change in local index of refraction.

LCoS phase modulators have a few performance limitations. For instance the number of pixels, the number of controllable gray levels [15] and a fringing field effect caused by the electric field applied on liquid crystals [16,17]. This fringing field is dependent on the voltage difference between nearby pixels, and limits mostly modulation in high spatial frequencies. In addition LCoS modulators are limited by the movement mechanism of the liquid crystal's and cannot exceed ~60 Hz. This drawback however is not so severe, since most of the application for signal processing do not need real time control. Lastly liquid crystals are polarization sensitive, only light with a certain polarization will interact with the liquid crystals. This can be overcome in a number of ways, such as by introducing a polarization diversity solution in the form of a walkoff crystal and a half-wave plate, such that the output light is divided to two co-propagating beams at the same polarization.

Despite these limitations which are out weighted by the advantages. In our PSP system we use a commercially available Holoeye Pluto LCoS phase modulator with high definition (HD) resolution of 1080×1920, pixels of 8 μm pitch, and total active size of 15.36×8.64 mm. Holoeye's phase SLM is designed especially for working in the near infrared (NIR) spectral region (around 1550 nm) and allows a phase modulation of up to 2π at this wavelength.

2.4 Calculation of Optical Resolution of Dispersive Elements

As was shown in previous sections, the capabilities of a PSP is dependent on its spectral dispersion element and SLM. We set a target resolution of 1 GHz for our proposed PSP. In this section we compare different bulk dispersive elements for their spectral characteristics, and assess how each might be used in order to meet the 1 GHz resolution target. The three dispersive optical elements being compared are: refractive glass prism, diffraction grating, and a phase array, as shown in Fig. 2.4.1.

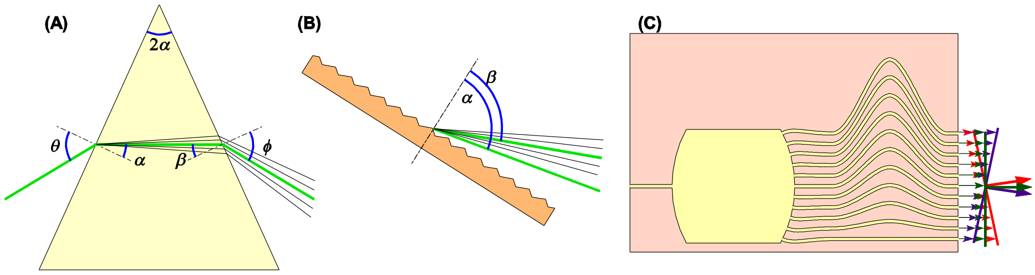

Fig. 2.4.1 – Dispersive elements being assessed for the task of resolving incident light to 1 GHz spectral bandwidth. (A) Prism, (B) Diffraction grating and (C) arrayed waveguide grating.

A. Prism angular dispersion analysis

Let's analyze for simplicity, the case of an isosceles prism, with equal incidence and refracted beam angles at the center wavelength. Using Snell's formulas of refraction at the input, $\sin(\theta)=n\sin(\alpha)$ and differentiating, we obtain: $dn\sin(\alpha)+n\cos(\alpha)d\alpha=0$. Likewise at the output, where $\sin(\phi)=n\sin(\beta)$ leads to $\cos(\phi)d\phi=dn\sin(\beta)+n\cos(\beta)d\beta$. Using the symmetry condition at center wavelength (*α*=*β*) and the fact that an internal angle change at one facet is opposite to the change at the other facet (*dα*=*dβ*), we can combine both equations to obtain: $\cos(\phi)d\phi=2dn\sin(\alpha)$ from which we can obtain the output angular dispersion:

$$\frac{d\phi}{d\lambda}=2\tan(\alpha)\frac{dn}{d\lambda}=2\tan\left(\arcsin\left(\frac{\sin(\theta)}{n}\right)\right)\frac{dn}{d\lambda} \tag{1.4.1}$$

From Eq. (2.4.1) the dispersion can grow to large values as *α*→90°. However *α* is the internal refraction angle, and can grow in magnitude up to the grazing incidence limit. We substitute *α* by the external angle of incidence. We see the angular dispersion depends linearly on the material dispersion and inversely on the refractive index. This dependency is similar to the Abbe number V_d defined by $V_d = \frac{n_D - 1}{n_F - n_C}$ which is a measure of a material dispersion, where n_D, n_F and n_C are the refractive indices of the material at the wavelengths of the Fraunhofer D, F and C spectral lines (589.3 nm, 486.1 nm and 656.3 nm respectively). Hence needed is a glass material with a small Abbe number. However, first the Abbe number which is defined for the visible spectrum has to be translated to the near infrared (NIR) (around 1.55 µm center wavelength) for telecom dispersion. From Fig. 2.4.2, we see that as glasses move farther from the ultra violet (UV) absorption edge, the refractive index variation decreases, which is opposite to the desired trend. The angular dispersion with the best dispersive glass for the near infrared IR (KzFS N_4) is 0.025 rad/µm.

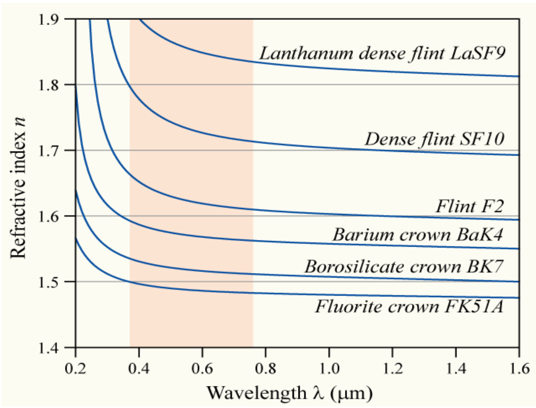

Fig. 2.4.2 – Refractive index of different types of glass at curtain wavelengths. At telecommunications wavelengths around 1.55 µm the refractive indexes drop, lowering the angular dispersion at the required wavelength.

For a resolution target 1 GHz (8 pm), first we calculate the angular separation between the two components at 0.2 µrad. Next we compare this angular bandwidth to the aperture divergence (λ/D). At λ=1.55 µm, we find the beam aperture necessary to resolve 1 GHz components as 7.75m!

B. Diffraction grating dispersion analysis

Now we analyze the dispersive properties of a diffraction grating. Again, for simplicity we shall assume a Littrow configuration (incidence and diffracted angles equal). Starting with the grating equation $\sin(\alpha)+\sin(\beta)=\lambda/\Lambda$ we differentiate to obtain the grating's angular dispersion:

$$\frac{d\beta}{d\lambda} = \frac{1}{\Lambda \cos(\beta)} \tag{2.4.2}$$

As β goes to grazing condition, the angular dispersion explodes. Since we assume Littrow mounting (α=β), we obtain $\Lambda = \lambda/2\sin(\beta)$, which leads to $d\beta/d\lambda = 2\tan(\beta)/\lambda$. Setting a practical value for β as 75° again, we obtain an angular dispersion of $4.82 \ \text{rad}/\mu\text{m}$.

For a resolution target 1 GHz (8 pm), we calculate the angular separation between the two components at 38.6 μrad. Next we compare this angular bandwidth to the aperture divergence (λ/D). At λ=1.55 μm, we find the beam aperture necessary to resolve 1 GHz components as 40mm. This is a much more reasonable value (compared to the prism), but still quite large for an optical component!

C: Phased array dispersion analysis

Let the phased array outputs be placed on a constant pitch, p, and have a path length difference $\Delta L=m\lambda_0/n_{eff}$. Associated with this path length difference is a phase delay at the design wavelength, λ_0, $\Delta\phi\ (\lambda_0)=K_0\cdot n_{eff}\cdot\Delta L=2\pi m$. Since the phase delay is an integer multiple of 2π, all waveguides are designed to radiate at the same phase outwards for the design wavelength. Next, let's examine the output phase dependence on wavelength.

$$\frac{d\phi(\lambda)}{d\lambda} = \frac{d}{d\lambda}\left(\frac{2\pi n_{eff}}{\lambda}\Delta L\right) = -\frac{2\pi m}{\lambda_0}\frac{n_g}{n_{eff}} \tag{2.4.3}$$

where n_g is the group index of the waveguides.

This wavelength-dependent phase results in the diffracted wave propagating with an angular dispersion of

$$\frac{d\theta}{d\lambda} = \arctan\left(\frac{d\phi/d\lambda}{k_0 p}\right) = \arctan\left(-\frac{m}{p}\frac{n_g}{n_{eff}}\right) \approx -\frac{m}{p}\frac{n_g}{n_{eff}} \tag{2.4.4}$$

The angular dispersion at the output of the phase array scales with m/p, suggesting we can increase the dispersion by decreasing the source pitch and increasing m which amounts to an increase in ΔL. However, ΔL (or m) cannot be increased without bound as it sets the free spectral range (FSR) of the phased array; defined by the wavelength range when the response repeats itself. The FSR is thus obtained

$$\Delta\lambda_{FSR}\frac{d\phi}{d\lambda} = 2\pi \quad \rightarrow \quad \Delta\lambda_{FSR} = \frac{\lambda_0^2}{\Delta L\cdot n_g} = \frac{\lambda_0}{m}\cdot\frac{n_{eff}}{n_g} \tag{2.4.5}$$

Assuming $n_{eff} \approx n_g$, the FSR is λ_0/m. If the phased array is to support a bandwidth covering the communication band (spanning ~35 nm), then $m \approx 1550/35 \approx 44$. However, since we wish to increase the angular dispersion, we can sacrifice bandwidth and thus obtain a larger m. Let's assume this bandwidth is 200 GHz or 1.6nm, then m can grow to ~935! Setting the waveguide pitch to 14μm, the obtained angular dispersion is now 69.14 rad/μm.

For a resolution target of 1 GHz (8 pm), we calculate the angular separation between the two components at 553.1 μrad. Next we compare this angular bandwidth to the aperture divergence (λ/D). At λ=1.55 μm, we find the beam aperture necessary to resolve 1 GHz components as 2.8mm. It is furthermore instructive to note that the beam aperture comprises N emitters at spacing p, or $D=N\cdot p$. We can thus establish that the spectral resolution is simply FSR/N, and for our 200GHz FSR and 1 GHz target resolution, we therefore require 200 waveguides in the phased array. This option can be realized with a Silica on Silicon planar light circuit (PLC). The device dimensions would be fairly compact ~ 4×5cm, smaller by far than the angular prism and diffraction grating.

It is necessary to mention that it is also possible to realize a virtual imaged phased array (VIPA), where its dispersion is based on multiple reflections from a thin plate with its back side coated with 100% reflection coating and the front side coated with a less than 100% reflection coating. The multiple outputs interfere resulting in spectral dispersion, where the width of the plate determines the FSR and the reflection of the surface determines its spectral resolution. The drawback in which makes VIPA not the preferred device for telecom applications is that the multiple virtual sources do not lie on the same plane, as result reducing the coupling efficiency when the light is coupled to a single mode fiber (SMF).

3 Experimental Setup and Results

3.1 Fine Resolution Arrayed Waveguide Grating Design

AWGs were originally developed for optical demultiplexing functionality in wavelength division multiplexing (WDM) systems [18-20]. An AWG demux employs a first star coupler (free space region) allowing an input waveguide to radiate into the waveguide array, followed by a second star coupler where the dispersed light emerging from the waveguide array is coupled to individual demultiplexed output waveguides (Fig. 3.1.1).

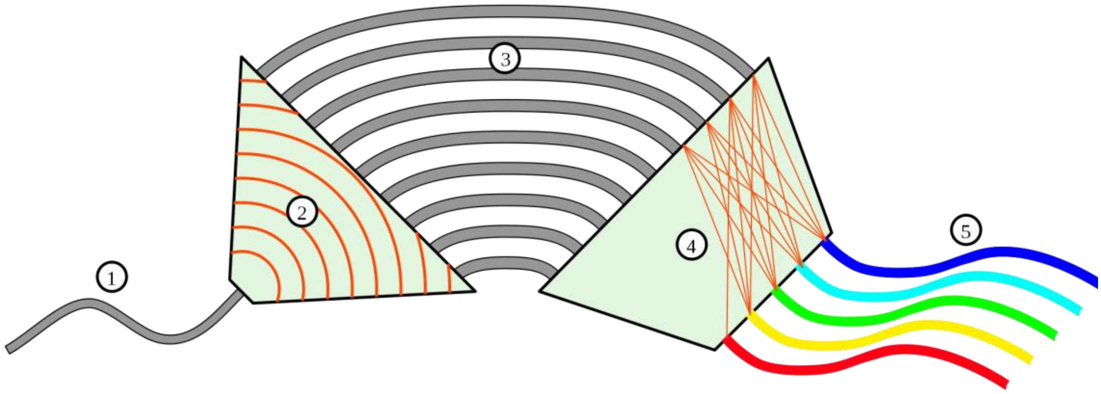

Fig. 3.1.1 – A schematic of an AWG: The input waveguide (1) radiates into a star coupler (2) which couples the light to the waveguide array (3) followed by a second star coupler (4) where the dispersed light emerging from the waveguide array is coupled to individual demultiplexed output waveguides (5).

Such demux AWGs are attractive in that they are compact, easily packaged and robust, due to guiding in high refractive index contrast waveguides allowing sharp bends on a planar lightwave circuit (PLC). The dispersive medium we utilize for our PSP application is an unconventional AWG, where we discard the second slab lens region that demultiplexes to output waveguides. The grating arms terminate at the PLC edge, allowing the light to radiate into free space. This forms a phased-array output that experiences angular dispersion on account of wavelength-dependent phase delays in the waveguide array. Using an external Fourier lens, we obtain spatially dispersed light allowing for manipulation in free space with an SLM.

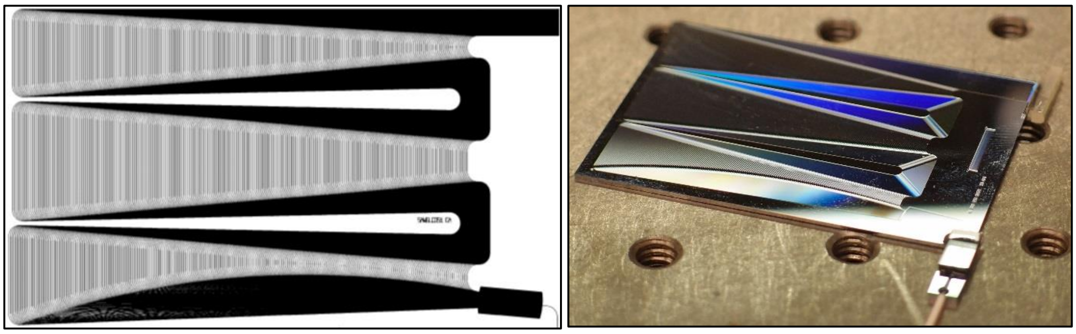

Fig. 3.1.2 – Arrayed Waveguide grating with sub-1 GHz optical resolution. (Left) Design layout (dimensions ~4×5cm). (Right) AWG with I/O fiber attached and cylindrical lens to collimate output radiating light in the guided (vertical) direction.

The key design features of an AWG are its incremental path length increase, ΔL, between successive waveguides and number of waveguides, N, within the array. The former sets the FSR according to $\nu_{FSR} = c/(\mathrm{n_{eff}} \cdot \Delta L)$ (where n_{eff} is the effective index of the waveguide propagating mode and c is the speed of light) and the latter sets the spectral resolution $\nu_{res} \cong \nu_{FSR}/N$. We set a target resolution for the AWG of 0.8 GHz leaving a margin of error for the PSPs set 1 GHZ resolution target. The AWG was designed with 200 GHz FSR and 250 waveguide arms to support spectral super-channels of 1 Tb/s capacity [21]. The AWG was implemented in a silica on silicon platform with 2% index contrast waveguides of 4×4 µm cross-section (Fig. 3.1.2-right) with n_{eff} =1.46. The AWG's N=250 waveguide arms have a relative path length difference of $\Delta L = m \cdot \lambda_0 / n_{eff}$ =~1mm (where m=935 is the diffraction order), for a total AWG path length difference of $N \cdot \Delta L$=250mm. The inverse of the time delay ($\Delta t = N \cdot \Delta L / v_g$=1.25ns) matches our 0.8 GHz target resolution, in line with time-bandwidth uncertainty principle. To obtain a compact AWG design for such a long path difference, the waveguides are folded three times within the PLC (total size is 5×4 cm) (Fig. 3.1.2-left). Light from an input waveguide excites the 250 waveguide arms via a confocal slab lens of ~8 mm radius. Power distribution across the waveguides was Gaussian, with edge waveguides approximately 20 dB lower power than central waveguides. The waveguides taper out at the slab lens to efficiently collect 75% of the input power. Following the slab lens, the waveguide arms are routed with differential lengths to the edge of the PLC (Fig. 3.1.2). Waveguide spacing within the AWG was chosen so that coupling between adjacent routes is negligible. The pitch p at the output (at the PLC edge) is 18.6µm, and the waveguides are adiabatically broadened to size Δ_{wg}=17µm. The optical field at the AWGs output facet is described by

$$E_{AWG}(\xi,\nu)=\sum_i a_i\cdot\phi\left(\frac{\xi-i\cdot p}{\Delta_{wg}}\right)\cdot\exp\left[j2\pi im\left(1+\frac{n_g}{n_{eff}}\cdot\frac{\nu-\nu_0}{\nu_0}\right)\right] \tag{3.1.1}$$

where a_i is the Gaussian apodization originating from AWG's star coupler (see dashed line in Fig. 3.1.3-top), $\phi(\bullet)$ represents a Gaussian mode of an individual waveguide located at $\xi=i\cdot p$, with an accumulated phase (argument of the exponent) that is dependent on the diffraction order, effective and group refractive indexes, and the optical temporal frequency. The phased array light output of the AWG at the PLC facet is Fourier transformed with lens f, yielding:

$$\mathrm{E}_{Fourier}(x,\nu)=\phi\left(\frac{\Delta_{wg}\cdot x}{\lambda_0\cdot f}\right)\cdot\sum_i\phi\left(\frac{x}{\Delta_{cw}}-\frac{\lambda_0\cdot f}{\Delta_{cw}\cdot p}\left(i+m+m\frac{n_g}{n_{eff}}\cdot\frac{\nu-\nu_0}{\nu_0}\right)\right) \tag{3.1.2}$$

where the Gaussian mode, ϕ , of the individual AWG's waveguides of size Δ_{wg}, determines the far field interference pattern envelope (the first term in Eq. (3.1.2), see dashed line in Fig. 3.1.3-bottom). The sum term is the constructive interference of the Gaussian apodized AWG output. Since the apodization is Gaussian, the constructive interference is too. Each spectral component creates multiple diffraction orders of size $\Delta_{cw}=4\cdot\lambda\cdot f/(\pi\cdot\Delta_{AWG})$ (where Δ_{AWG} is the AWG output mode size), their spacing being inversely proportional to the waveguide array pitch, p. The number of excited diffraction orders depends on the extent of the far field interference pattern envelope. Hence having narrow waveguides relative to the waveguide pitch would undesirably result in the excitation of many diffraction orders. To minimize the diffraction order excitation count, we adiabatically broaden the waveguides at the AWG output from Δ_{wg}=4 µm to Δ_{wg}=17 µm, on p=18.6 µm pitch.

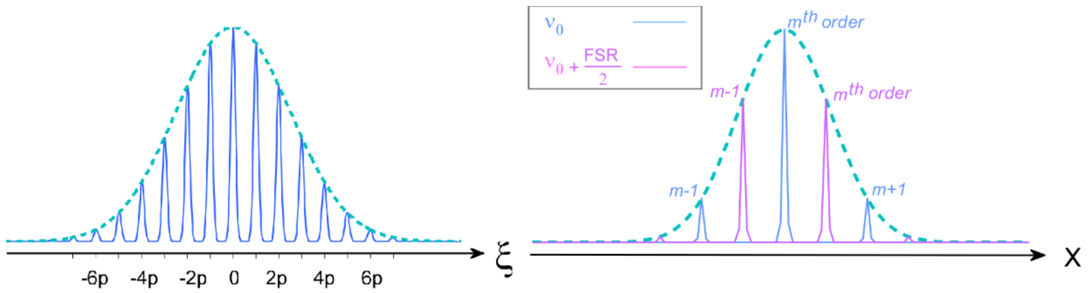

Fig. 3.1.3 – (Top) Depiction of Gaussian apodization of an AWG output with a waveguide pitch *p*. (Bottom) The Fourier transform of AWG output, where the envelope is the Fourier transform of a single waveguide Gaussian mode. The diffraction orders exist underneath this curve. Blue: Diffraction orders at the designed ν_0 frequency. Purple: Diffraction orders at the ν_0 + FSR/2 frequency.

From Eq. (3.1.2) we calculate the spatial dispersion by simple differentiation:

$$\frac{dx}{d\nu} = \frac{c \cdot m \cdot f}{\nu_0^2 \cdot p} \cdot \frac{n_g}{n_{eff}} \tag{3.1.3}$$

Our Fourier transform lens is of f=50 mm, thus obtaining spatial dispersion of 20 μm·GHz^{-1}. For efficient coupling to the input/output fiber, a mode converter section was used to match the mode shapes of the 4×4μm waveguide and the single mode fiber. Fiber to PLC coupling loss of -0.5dB was achieved. A total loss (one way) of ~2dB was observed. This additional loss derives mostly from the star coupler in the AWG design. The PLC facets were polished, and a 1.5 mm focal length high NA cylindrical lens was attached at the output facet to collimate the light in the guided (vertical) direction.

The far field radiation from the AWG should be spectrally resolved, as predicted by Eq. (3.1.2), and allow filtering by a SLM. In practice, we did not observe a spectrally resolved signal due to phase errors on each waveguide. Many factors may contribute to the sources of phase errors, such as lithography/etching errors, core height variations, refractive index inhomogeneity and/or stress. To overcome lithography/etching imperfections (Fig. 3.1.4) a scheme is needed to phase correct each individual waveguide, ensuring the constructive inference at the designed wavelength to be observed in the spectral plane.

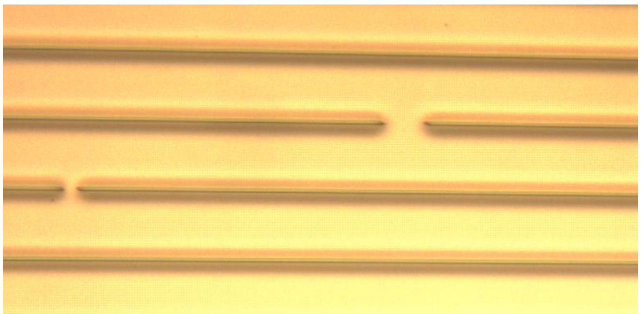

Fig. 3.1.4 – A microscope image of one of our designed AWGs with severe lithography/etching imperfections resulting in non-propagating waveguides.

3.2 Active Phase Error Compensation with an LCoS SLM

To circumvent the phase error problem, we devised an optical arrangement that images the PLC output facet onto an LCoS SLM at a secondary plane with a magnification factor of M=3 (Fig. 3.2.1). This magnification factor was chosen to map the AWG array output width (18.6 μm×250=4.65 mm) to ~14 mm, efficiently spanning the LCoS SLM width (Holoeye Pluto, 1920×1080 pixels at 8 μm/pixel=15.36×8.64 mm). The waveguide pitch of 18.6 μm is magnified to 55.8 μm, equaling 7 pixels on the SLM. Each waveguide output mode occupies a unique position on the SLM, and by applying a voltage onto the unique regions we can modulate the phase of the individual reflected light beams. The 7 pixel span also helps reduce the fringe field impact between adjacent LCoS pixels at different voltage setting. The reflected light from the image plane is then Fourier transformed onto the spectrally resolved plane. If we properly adjust the phases of each output waveguide, then the constructive interference pattern of all waveguides should focus to a tight spot (for continuous wave (CW) excitation) with higher order diffraction modes (per. Eq. 3.1.2). Different wavelengths that accumulate differential phases from each waveguide, will also focus to a tight spot yet displaced due to the linear phase variation across the array, thereby achieving the spatial dispersion. Our free-space solution currently supports one polarization state, but polarization diversity can be easily introduced to handle both polarization states which has not been attempted in this work.

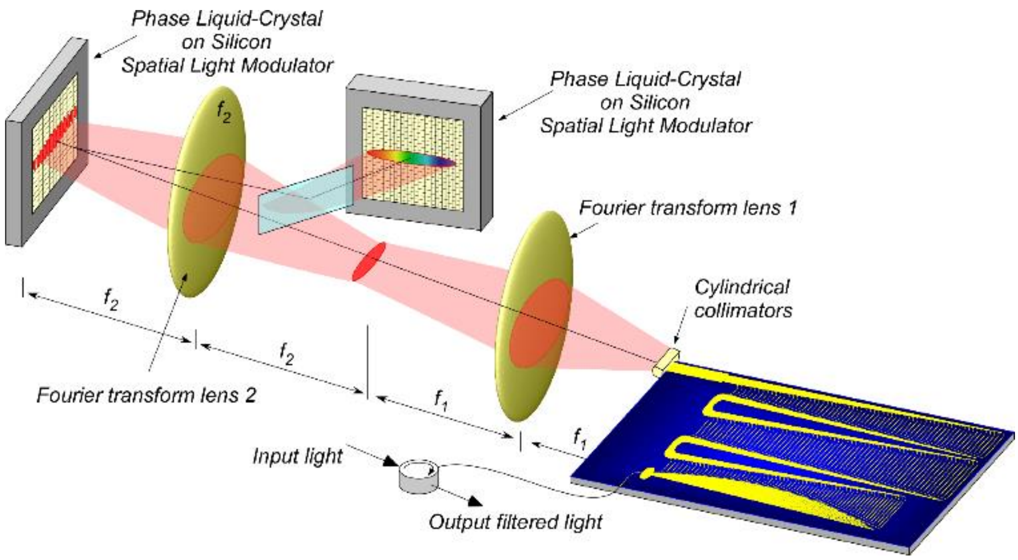

Fig. 3.2.1 – Experimental setup for compensation of AWG phase errors with an LCoS phase modulator and spectral processing in the Fourier plane.

The procedure to set the phases starts with placing an infrared (IR) camera instead of the LCoS SLM at the image plane to directly observe the PLC output facet (Fig. 3.2.2- top). The image of the output waveguide array is observed. The waveguide modes are vertically elongated due to the cylindrical collimation lens affixed to the PLC. The intensity of light is Gaussian distributed, as expected through a slab lens excitation, with few waveguides exhibiting excess loss due to lithography imperfections. These amplitude variations, amounting to the a_i terms of Eq. 3.1.1, can modify the constructive mode shape at the Fourier plane. Since they are few their impact is minimal.

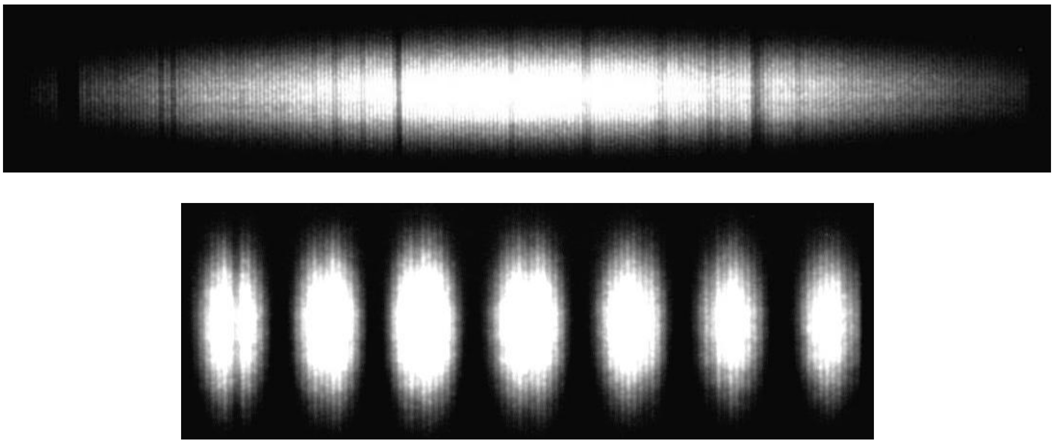

Fig. 3.2.2 – (Top) Direct image of light at the PLC output facet. Vertical axis is stretched due to cylindrical collimating lens. (Bottom) Direct image of the polarization interference pattern formed by the different propagation constants.

Prior to phase correcting one of the AWG's polarizations with an LCoS SLM, it is crucial to confirm that the AWG maintains polarization. In order to check this, we introduce linearly polarized white light through the AWG and add a free space polarizer between the two Fourier lenses in our setup. The polarizer was aligned to the horizontal polarization matching one of the primary AWG polarizations and the only LCoS SLM supported polarization. When the polarized white light was aligned with the free space polarizer, maximum power fell on the camera resulting in all waveguides having the same intensity polarization-wise (Fig. 3.2.2). The power became null when the free space polarizer was set to the vertical polarization. This result confirms that the AWG in fact does maintain polarization. If an intensity periodicity was seen that would indicate that the AWG does not maintain polarization, which fortunately is not the case. Moreover we can deduce horizontal and vertical effective refractive indexes differences. This was done by setting both polarizer and the AWG's output to be comprised of equal horizontal and vertical polarization states Eq. (3.2.1), resulting with the intensity captured on the camera according to Eq. (3.2.2).

$$E_{wg} = A_0 \cdot \cos(\theta) \cdot \exp[-j \cdot \beta_x \cdot z]\hat{x} + A_0 \cdot \sin(\theta) \cdot \exp[-j \cdot \beta_y \cdot z]\hat{y} \quad (3.2.1)$$

$$I_{wg} = |E_{wg}|^2 = 2 \cdot A_0^2 \cdot \cos^2\left((\beta_x - \beta_y) \cdot \frac{z}{2}\right) \quad (3.2.2)$$

Where $A_0\, cos(\theta)$ and $A_0\, sin(\theta)$ represent horizontal and vertical polarization amplitudes respectively of an individual waveguide. For equal amplitudes θ was set to 45^0.The respective propagation constants $\beta \approx 2\pi \cdot n_{eff}/\lambda$. $n_{eff,x}$ and $n_{eff,y}$ should be equal by virtue of the square waveguide profile though due to fabrication imperfections this is not true.

In Fig 3.2.2 it can be seen that there is an interference pattern Eq. (3.2.2) caused by the different effective indexes of the horizontal and vertical polarizations. From the inference pattern we can measure the beating to be about 105 camera pixels wide, roughly equaling 18 waveguides (N_{beat}). Multiplying the periodicity by the AWG's ΔL (1 mm) around λ=1.55 μm, the deference between effective indexes can be calculated to be $\Delta n_{eff}=2 \cdot \lambda/(N_{beat} \cdot \Delta L) \approx 1.7 \cdot 10^{-4}$.

Next we placed the LCoS SLM at the AWG image plane and moved the camera to the Fourier plane (in place of the SLM seen in Fig. 3.2.1). The locations of the individual waveguides on the SLM pixels were registered by writing a phase ramp pattern five pixels wide (to tilt the light falling on the SLM towards the pickup mirror and spectral plane) and scanning it across the SLM while registering the power reaching the camera, from which we were able to deduce the waveguides center locations (Fig. 3.2.3).

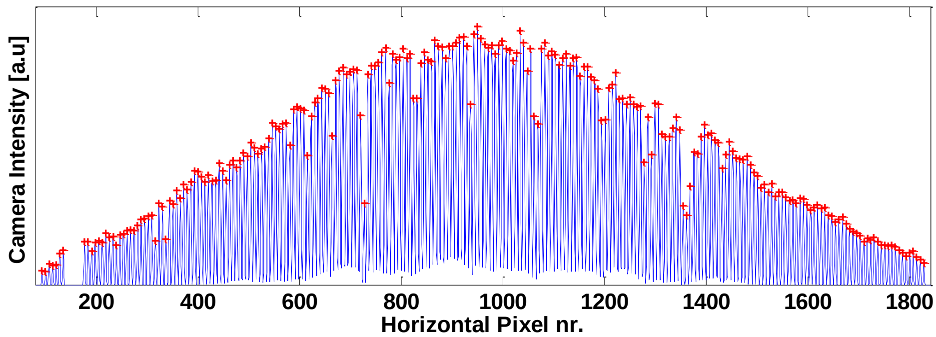

Fig. 3.2.3 – Location of waveguides on SLM. A few waveguides have imperfections effecting light transmission through them.

Afterwards, we broaden the rectangle to capture two waveguides modes (14 pixels wide), and examine the interference pattern of the two selected waveguide per Eq. (3.1.2) in the Fourier plane for each successive waveguide pair:

$$\mathrm{I} = \left|F\left(E_{i,k}\right)\right|^2 \propto \phi\left(\frac{2\cdot\Delta_{wg}\cdot x}{\lambda_0\cdot f}\right)\cdot\cos^2\left(\pi m\left(1+\frac{n_g}{n_{eff}}\cdot\frac{\nu-\nu_0}{\nu_0}\right)+\left(\frac{\phi_i-\phi_k}{2}\right)+\frac{p\cdot x\cdot\nu_0}{f\cdot c}\right) \qquad (3.2.3)$$

where the Gaussian mode, $\phi(\bullet)$, of the individual AWG's waveguides of size Δ_{wg}, determines the far field interference pattern envelope and the interference phase is dependent on the ϕ_i, ϕ_k respected waveguides phase errors

This is analogous to Young's double slit experiment; when the waveguides are in phase the interference pattern forms a dominant central lobe and a weak side lobe on each side. When the two waveguides are out of phase (shifted by π), the interference pattern is that of two equal peaked lobes (with a null in the center). Images of these interference patterns collected by the camera are shown in Fig. 3.2.4.

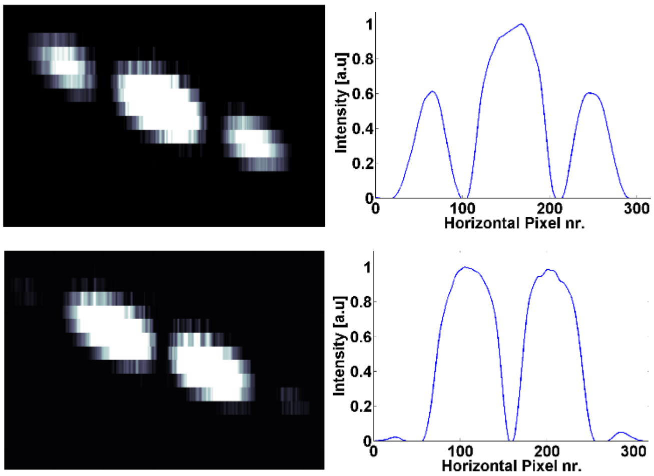

Fig. 3.2.4 – Interference pattern of a waveguide pair of the imaged PLC observed at the Fourier plane camera, used to bring the waveguides into identical phase. Waveguide pair in phase (Top) and π out of phase (Bottom).

By modifying the reflected phase of each waveguide from the image plane SLM, we set every waveguide pair under test to be in equal phase by examining the far field interference. This is done by adding a phase offset to a particular beam in addition to the 7 pixel wide phase ramp during interference between two beams. All the waveguide's phases were set to reflect a constructive interference using this technique. This procedure starts from the center waveguide, and proceeds right to the array edge one waveguide at a time to set equal phase as the predecessor, and then correcting the left half starting from the center in the same manner. Greatest sensitivity was obtained by comparing the area beneath the two side peaks.

When encountering an inactive waveguide (no light emerging), the interference is collected between the waveguides before and after the inactive zone. This increases the spatial modulation frequency on the far field beam, but the symmetry criterion can still be identified, to maintain phase continuity across the gap.

The phase corrections that are required for each waveguide are thus completely known and can now be applied simultaneously on the LCoS SLM to correct the phase response of the entire AWG output. The correction values and the LCoS phase pattern are shown in Fig. 3.2.5.

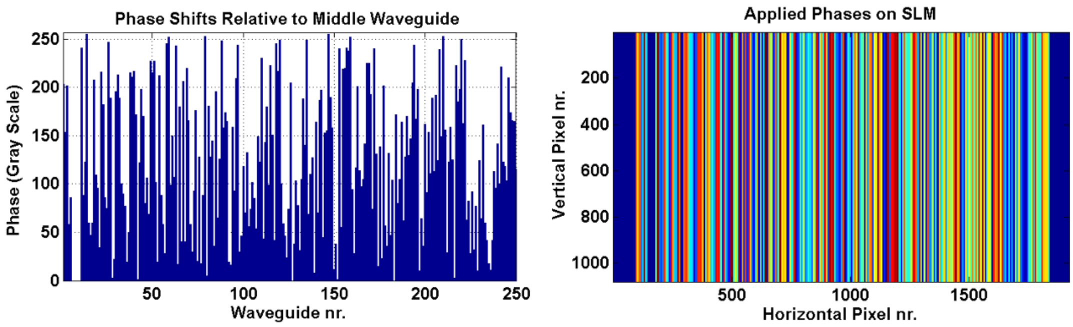

Fig. 3.2.5. – (Left) Waveguide phase errors relative to the centermost waveguide. (Right) All waveguides phase shift pattern written to the SLM.

These phase corrections appear quite random, spaced between 0 and 2π across the array (with possible multiples of 2π which we cannot distinguish). These phase errors are the explanation as to why the phased array did not function as planned, as they constitute a random phase realization as opposed to equal phase, and the far field pattern of a random phase distribution is spread out instead of focusing to a spot. One of the advantages of the phase correction with the LCoS SLM is that we can independently access each waveguide with one single device. Alternatively, one could place individual thermo-optic (TO) modulators on each waveguide to phase correct them one by one [22]. However, such TO modulators are power hungry, and can cause thermal crosstalk between adjacent waveguides. Similarly the waveguide array could be implemented in electro-optic waveguide material, allowing electrical tuning [23]. Still electro-optic tuning typically operates over single polarization. In the free-space solution we employed, it is possible to treat each polarization separately by introducing a polarization diversity solution in the form of a walkoff crystal and a half-wave plate, such that the output light is divided to two co-propagating beam arrays of the same polarization. The imaging arrangement would observe two sets of AWG outputs, one per polarization.

With the camera still mounted at the Fourier plane, we can now directly observe the far field radiation pattern of the entire array (as opposed to the pair-wise radiation pattern of Fig. 3.2.4). When phase corrections are applied, the far field pattern constructively focuses to a spot with the corresponding higher orders (Fig. 3.2.6). Tuning the center wavelength causes the focus spot position to shift, linearly with wavelength, in accordance with the spatial dispersion. If we turn off the LCoS phase compensation and directly image the cumulative far field radiation pattern (with the phase errors), we observe a random, speckle-like interference pattern spanning a wide field, which still shifts in location with wavelength, but is not spectrally resolved.

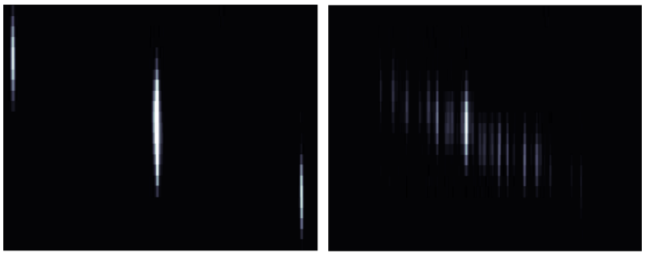

Fig. 3.2.6 – Far field radiation patterns for CW excitation laser wavelength. (Left) with applied phase correction. (Right) without phase correction.

3.3 Fine Resolution PSP Characterization

To complete the PSP construction, we replace the IR camera at the spectral plane with a second LCoS SLM to return all the light back to the first LCoS SLM and then to the AWG and output fiber. The SLM was placed at a slight tilt diverting all light out the optical path (to eliminate the cover glass back reflection). An attenuation look up table was created to calibrate the linear phase ramp on the SLM for a selected coupling loss. The look-up table was made by locating the beams center on the SLM by a 0/π phase step scan (see Appendix), then proceeding to register the attenuation from different linear phase ramps (angles). With regards to the look-up table a linear phase ramp function was written on the SLM in order to steer back selected spectral components with desired attenuation and phase. Since each spectral component excites few diffraction orders, we back reflect them all to collect all the energy. This is done by repeating the frequency selection pattern on the SLM with offsets corresponding to the diffraction orders (Fig. 3.3.1). The diffraction orders are spatially separated by $\lambda_0 \cdot f/p$ equaling 521 LCoS pixels (see Eq. (3.1.2)). Selecting a frequency band in this manner achieves uniform performance no matter where the frequency band occurs with respect to the center frequency of the AWG (Fig. 3.3.2-Left).

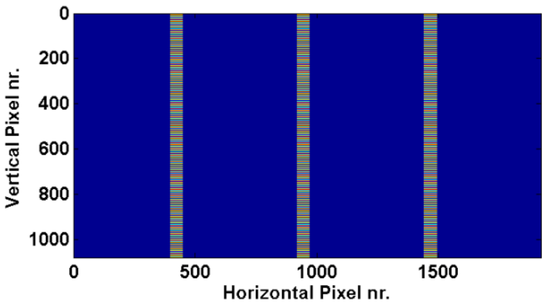

Fig. 3.3.1 – Phase function written to the SLM, for selecting 20GHz band, including left and right diffraction orders.

In our PSP implementation the LCoS pixel size is 8μm and the spatial dispersion equals 20 μm·GHz^{-1} yielding 400 MHz addressability for our PSP (Fig. 3.3.2-Left).

All our PSP characterization was performed with a swept laser interferometry technique (using a Luna Technologies optical vector analyzer), as instruments such as grating based optical spectrum analyzers do not offer sufficient spectral resolution. The 0.8 GHz spectral resolution was confirmed by measuring the 90-10 transition bandwidth, which is in line with the resolution definition $\nu_{res}=(\Delta_{cw}/2)/(dx/d\nu)$ where

Δ_{cw}=32 µm. Thus beating the 1 GHz resolution target set for our PSP. The focused spectral spot shows some deviation from a smooth Gaussian characteristic (defined by Eq. (2.2.3)) as witnessed by a lobe in the transition band occurring about -20 dB down (Fig. 3.3.2-Right). This may be due to imperfect phase compensation or the amplitude deviations from Gaussian apodization. The pixel to frequency mapping shows that a 400 MHz addressability was obtained.

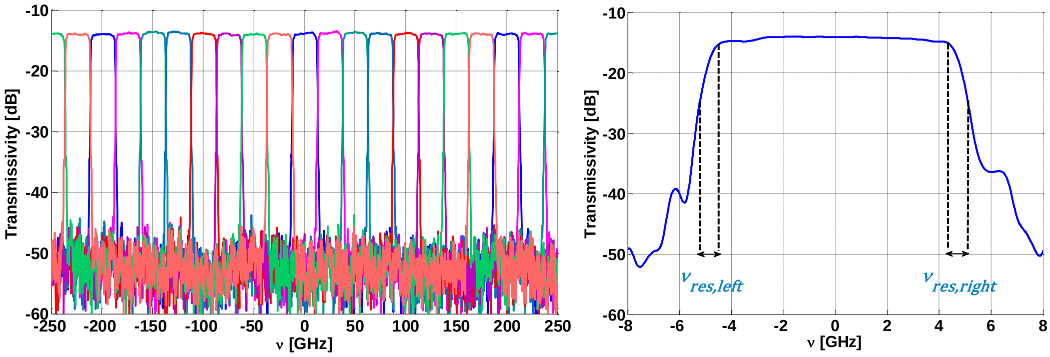

Fig. 3.3.2 – Optical band selection: (Left) Selection of 25 GHz wide bands within the 200 GHz FSR with 400 MHz addressability. (Right) Resolution metrics of 0.8 GHz, measured from -0.5dB (10%) down to - 10dB (90%).

With this current setup (Fig. 3.3.3) the measured loss is -14 dB. The identified loss mechanisms are as follows: AWG fiber coupling efficiency (×2) -6 dB, LCoS SLM (×3) -4 dB and Optical circulator (×2) -2 dB. The total known loss amounts to -12 dB, leaving unaccounted losses of 2 dB that are likely from inefficiency of optical collimation and focusing back to AWG. We also observe that our dispersed spectra is slanted in all our images (Figs. 3.2.4 and 3.2.6). This is most likely due to a small roll angle between the attached cylindrical lens and the PLC, which probably accounts for some of the unaccounted losses.

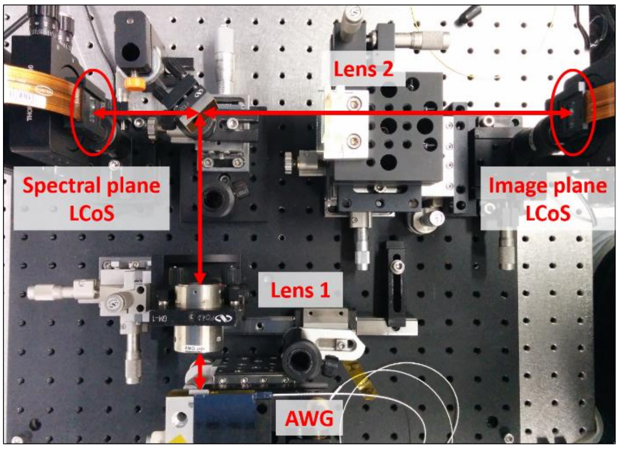

Fig. 3.3.3 – Photo of the experimental setup for compensation of AWG phase errors with an LCoS phase modulator and spectral processing in the Fourier plane.

3.4 Fine Resolution PSP Capabilities Demonstration

In order to demonstrate the capabilities of the fine resolution processor, we display an array of filtering functions that are relevant to processing optical communication signals. These functions were demonstrated using a Luna Technologies optical vector analyzer to represent the optical responses of the PSP functions on a telecom signal.

No matter the type of telecom signal that is being implemented, whether it being orthogonal frequency division multiplexing (OFDM) or Nyquist WDM. The signals are generated by optical modulators deriving from digital to analog converters (DAC) which have a different response according to frequency. To overcome this problem in order to process a signal more efficiently it is possible to shape a signal's bandwidth so that all frequencies have the same optical signal to noise ratio (OSNR). It is possible by imposing upon a signal the inverse DAC response to equalize the frequency dependence throughout the channel (Fig. 3.4.1-Bottom).

These signals may have different allocated bandwidths that have to be individual processed before transmission in long haul systems. Before transmitting the signal, it has to be cut to the specific bandwidth, discarding unwanted DAC signal harmonic images on either side of the allocated channel bandwidth. In Fig. 3.4.1-Top we display various bandwidth filtering with in the designed 200 GHz FSR. Any number of filtering windows with various bandwidths can be placed with 400 MHz accuracy in the dedicated FSR.

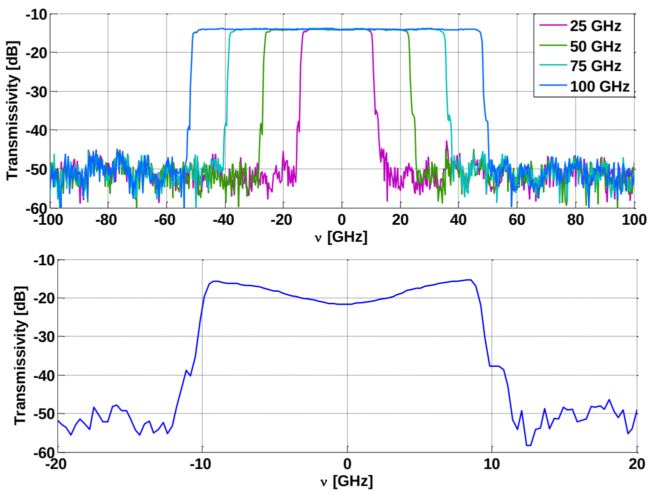

Fig. 3.4.1 – (Top) Various rectangular bandwidth filtering, for simplicity all channels were filtered around the same central frequency

(Bottom) A 20 GHz passband with an attenuation function $1\text{-}0.6 \cdot \sin(v - v_0)$ **in order to equalize the DAC inhomogeneous response.**

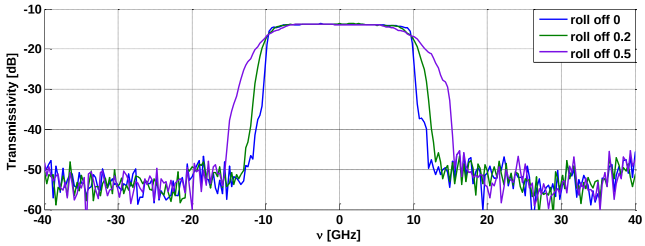

Fig. 3.4.2 – Nyquist-shaping via optical filtering: 20 GHz raised cosine filter with assorted roll off factors.

Another pulse shaping technique that we can implement with our PSP is a raised cosine filter (Fig. 3.4.2) for Nyquist-WDM. Where the gradient of the transmission function known as the roll off factor, is a measure of the excess bandwidth of the filter channel.

Finally we demonstrate the pinnacle capability of the fine resolution PSP. The ability to filter out sub carriers from a full channel. We show OFDM single sub – carrier optical drop-demux, “cherry-picking” of individual OFDM subcarriers out of a 20 GHz full channel. The PSP was programmed for sinc shaped matched optical filtering of the imagined signal consisting of 5, 8 or 12 subcarriers at 4, 2.5 and 1.5 GHz respective spacings (Fig. 3.4.3-Top). In addition to matched OFDM sub carrier demux we also show rectangular filtering of a 20 GHz full with sub – carries spaced 1.25 GHz, the pass bandwidths varying 4, 2 and 1.6GHz (Fig. 3.4.3-Bottom).

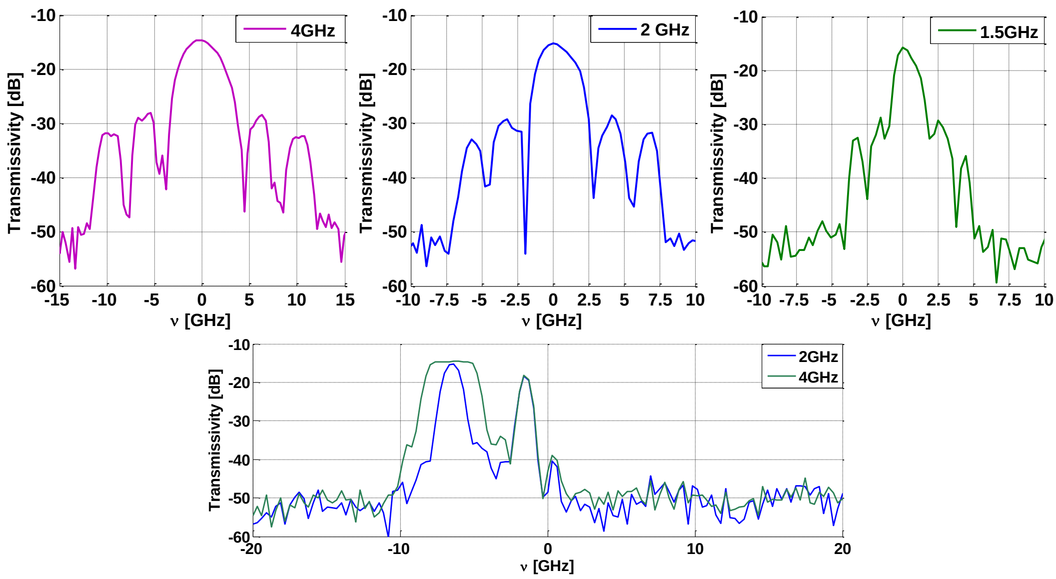

Fig. 3.4.3 – (Top) OFDM optical Sinc-shaped demultiplexing, optical filters ranging from 4 GHz down to a narrow 1.5 GHz spacing filter. (Bottom) Rectangular filtering with bandwidths of 4 and 2 GHz. A pass band of 1.6 GHz which is the smallest window that can be opened with our PSP is placed 5 sub bands away as a comparison to the other passbands.

3.5 Discussion and Conclusions

We have introduced the concept of a photonic spectral processor and how its abilities are characterized as a function of resolution and addressability. Both characterization techniques were defined in addition to the methods of calculating and measuring them. The sub-GHz resolution goal which was set for our PSP was a guideline for choosing the preferred chromatic dispersion element. Several dispersion elements were compared resulting with the AWG as the favored element to implement the fine resolution PSP. Shown in this work was a record performance metric AWG design with a 200 GHz FSR capable of resolving sub-one GHz resolution spectral features.

Due to fabrication imperfections a phase correction strategy had to be applied to the light beams emerging from the 250 waveguides of the AWG output. These phase errors rendering the AWG unusable in a fine resolution PSP were successfully phase corrected with a novel phase SLM compensation scheme. This was done with an LCoS SLM placed in an imaging configuration where all 250 waveguide phase errors were measured and corrected posterior to the AWGs fabrication.

With a second LCoS SLM located at the Fourier plane we utilized our PSP in different spectral amplitude and phase manipulation experiments, showing a myriad of optical processing capabilities. We successfully demonstrated optical functions such as flexible spectral shaping and sharp sub-carrier drop demultiplexer with sub-GHz spectral resolution.

It is now possible to implement our fine resolution PSP with telecom signals performing complex spectral filtering for channel selection, dispersion compensation, and signal shaping.

4. References

1. M. A. F. Roelens, S. Frisken, J. A. Bolger, D. Abakoumov, G. Baxter, S. Poole, and B. J. Eggleton, “Dispersion Trimming in a Reconfigurable Wavelength Selective Switch,” *J. Lightwave Technol.* **26**, 73-78 (2008).
2. R. Schmogrow, S. Ben-Ezra, P. C. Schindler, B. Nebendahl, C. Koos, W. Freude, and J. Leuthold, “Pulse-Shaping With Digital, Electrical, and Optical Filters—A Comparison,” *J. Lightwave Technol.* **31**, 2570-2577 (2013).
3. H. Hu, D. Kong, E. Palushani, M. Galili, H. C. H. Mulvad, and L. K. Oxenløwe, “320 Gb/s Nyquist OTDM received by polarization-insensitive time-domain OFT,” *Opt. Express* 22, 110-118 (2014).
4. D. M. Marom, D. T. Neilson, D. S. Greywall, C.-S. Pai, N. R. Basavanhally, V. A. Aksyuk, D. O. López, F. Pardo, M. E. Simon, Y. Low, P. Kolodner, and C. A. Bolle, “Wavelength-Selective 1 x K Switches Using Free-Space Optics and MEMS Micromirrors: Theory, Design, and Implementation,” *J. Lightwave Technol.* **23**, 1620-1630 (2005).
5. Frisken, S.; Poole, S.B.; Baxter, G.W., “Wavelength-Selective Reconfiguration in Transparent Agile Optical Networks,” *Proc. IEEE* **100**, 1056-1064 (2012).
6. D. Sinefeld and D. M. Marom, “Hybrid Guided-Wave/Free-Space Optics Photonic Spectral Processor Based on LCoS Phase Only Modulator,” *Photon. Technol. Lett.* **22**, 510-512 (2010).
7. D. Sinefeld, S. Ben-Ezra, D. M. Marom, “Nyquist-WDM filter shaping with a high-resolution colorless photonic spectral processor,” *Opt. Lett.* **38**, 3268-3271 (2013).
8. M. Shirasaki, “Chromatic dispersion compensator using virtually imaged phased array,” Photon. Technol. Lett. 9(12), pp. 1598-1600 (1997).
9. K. Takada, M. Abe, T. Shibata, and K. Okamoto, “1-GHz-Spaced 16-Channel Arrayed-Waveguide Grating for a Wavelength Reference Standard in DWDM Network Systems,” *J. Lightwave Technol.* **20**, 850-853 (2002).
10. D.T. Neilson et al, “MEMS-based channelized dispersion compensator with flat passbands,” IEEE J. Lightwave Technol. 22, 101-105 (2004).

11. D. T. Neilson, et al., “Channel equalization and blocking filter utilizing microelectromechanical mirrors,” IEEE J. Select. Top. Quant. Electron. vol. 10, no. 3, pp. 563- 569, May-June 2004.
12. J. Dunayevsky, D. Sinefeld, and D. Marom, "Adaptive Spectral Phase and Amplitude Modulation Employing an Optimized MEMS Spatial Light Modulator," in Proc. OFC, paper OM2J.5 (2012).
13. Boskovic, M. Sharma, N. Antoniades, M. Lee “Broadcast and Select OADM nodes Application and Performance Trade-offs”, in Proc. OFC, paper TuX2 (2002).
14. Soutar and K. H. Lu, "Determination of the physical properties of an arbitrary twisted-nematic liquid crystal cell" Opt. Eng. 33 2704–12 (1994).
15. Sinefeld and D. M. Marom, "Insertion Loss and Crosstalk Analysis of a Fiber Switch Based on a Pixelized Phase Modulator," J. Lightwave Technol. 29, 69 - 77 (2011).
16. X. Wang, B. Wang, P. J. Bos, J. E. Anderson, J. J. Pouch, and F. A. Miranda, “Finite-difference time-domain simulation of a liquid-crystal optical phased array,” J. Opt. Soc. Am. A 22, 346-354, (2005).
17. K. H. Fan-Chiang, S. T. Wu and S.H. Chen, "Fringing-field effects on high-resolution liquid crystal microdisplays," Display Technology, Journal of, 1, 304-313, (2005).
18. C. Dragone, “An N*N optical multiplexer using a planar arrangement of two star couplers,” *Photon. Technol. Lett.* 3, 812-815 (1991).
19. K. Okamoto, K. Takiguchi, and Y. Ohmori, “16-channel optical add/drop multiplexer using silica-based arrayed-waveguide gratings,” Electron. Lett. 31, 723-724 (1995).
20. L. H. Spiekman, M. R. Amersfoort, A. I. de Vreede, F. P. G. M. van Ham, A. Kuntze, J. W. Pedersen, P. Demeester, M. K. Smit, “Design and realization of polarization independent phased array wavelength demultiplexers using different array orders for TE and TM,” J. Lightwave Technol. 14, 991-995 (1996).
21. D. Klonidis, S. Sygletos, D. M. Marom, S. Fabbri, A. Ellis, E. Pincemin, C. Betoule, G. Thouenon, D. Hillerkuss, B. Baeuerle, A. Josten, J. Leuthold, J. Zhao, S. Ben-Ezra, J. F. Ferran, M. Angelou, G. Papastergiou, P. Zakynthinos, I. Tomkos, “Enabling transparent technologies for the

development of highly granular flexible optical cross-connects," 16^{th} Int. Conf. Transparent Optical Networks (ICTON) 2014.

22. J. Doylend, M. R. Heck, J. Bovington, J. Peters, L. Coldren, and J. Bowers, "Free-space Beam Steering in Two Dimensions Using a Silicon Optical Phased Array," in Proc. Optical Fiber Communication (OFC) Conference 2012, paper OM2J.1.
23. T. McDermott and T. Brewer, "Large scale IP router using a high speed optical switch element," JON 2, 229-240 (2003).

Appendix: Locate Gaussian Centroid Technique

A useful technique for locating the center of a Gaussian beam on a phase SLM device is by applying a phase pattern step function. The step function consists of an upper phase level π and a lower phase level zero written onto the LCoS. The transition coordinate of these two levels is changed incrementally in a scanning fashion resulting in interference between the two coupled Gaussian parts. Complete destructive inference occurs when the transition point is aligned with the center of the Gaussian. The calculation, which shows the intensity corresponding to the transition coordinate can be done by taking a Gaussian beam:

$$\mathrm{E}(x) = \left(\frac{2}{\pi \cdot w_0^2}\right)^{\frac{1}{4}} \cdot \exp\left[\frac{-x^2}{w_0^2}\right]$$

where $2w_0$ is the full width of the electrical field at 1/e and calculating the overlap integral of the two Gaussian parts with a phase step $\Phi(x-x')$.

$$I = \int_{-\infty}^{\infty} E(x)\Phi(x-x')E(x)dx = \left(\frac{2}{\pi \cdot w_0^2}\right)^{\frac{1}{2}} \cdot \int_{-\infty}^{\infty} \exp\left[\frac{-x^2}{w_0^2}\right] \cdot \exp\left[j\pi \cdot Step(x-x')\right] \cdot \exp\left[\frac{-x^2}{w_0^2}\right] dx$$

$$= \left(\frac{2}{\pi \cdot w_0^2}\right)^{\frac{1}{2}} \cdot \left[\int_{x'}^{\infty} \exp\left[\frac{-2x^2}{w_0^2}\right] dx - \int_{-\infty}^{x'} \exp\left[\frac{-2x^2}{w_0^2}\right] dx\right] = \left(\frac{2}{\pi \cdot w_0^2}\right)^{\frac{1}{2}} \cdot \int_{x'}^{\infty} \exp\left[\frac{-2x^2}{w_0^2}\right] dx - \left[1 - \left(\frac{2}{\pi \cdot w_0^2}\right)^{\frac{1}{2}} \cdot \int_{x'}^{\infty} \exp\left[\frac{-2x^2}{w_0^2}\right] dx\right]$$

$$= 2 \cdot \left(\frac{2}{\pi \cdot w_0^2}\right)^{\frac{1}{2}} \cdot \int_{x'}^{\infty} \exp\left[\frac{-2x^2}{w_0^2}\right] dx - 1 \xrightarrow[y=\frac{\sqrt{2}}{w_0},\, dy=\frac{\sqrt{2}}{w_0}dx,\, x' \to \frac{x'\sqrt{2}}{w_0}]{} = \frac{2}{\sqrt{\pi}} \cdot \int_{\frac{x'\sqrt{2}}{w_0}}^{\infty} \exp\left[-y^2\right] dx - 1 = erf\left[\frac{x'\sqrt{2}}{w_0}\right] - 1$$

The overlap integral yields an error function (Fig. 1) by which the center of the beam can be located on the SLM as the transition pixel where minimum intensity is registered.

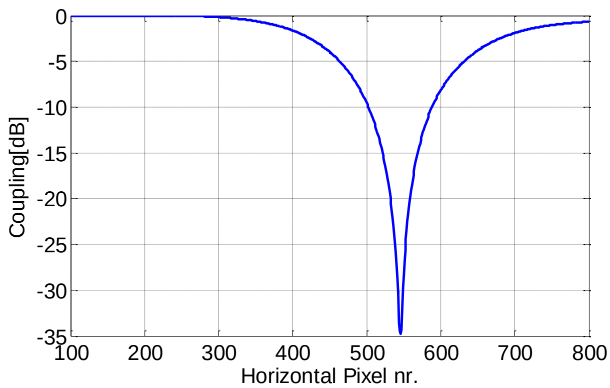

Fig. 3.4.2 – A horizontal 0/π phase step scan with a Holoeye Pluto LCoS SLM. The beams center was located at pixel number 547.